Long spin diffusion length in few-layer graphene flakes

W. Yan[1†], L. C. Phillips[1], M. Barbone[2], S. Hämäläinen[3], A. Lombardo[2], M. Ghidini[1,4], X. Moya[1], F. Maccherozzi[5], S. van Dijken[3], S. S. Dhesi[5], A. C. Ferrari[2] and N. D. Mathur[1,*]

[1]Department of Materials Science, University of Cambridge, Cambridge, CB3 0FS, UK.

[2]Cambridge Graphene Centre, University of Cambridge, Cambridge CB3 0FA, UK.

[3]NanoSpin, Department of Applied Physics, Aalto University School of Science, P.O. Box 15100, FI-00076 Aalto, Finland.

[4]DiFeST,University of Parma, viale G.P. Usberti 7/A, 43124 Parma, Italy.

[5]Diamond Light Source, Chilton, Didcot, Oxfordshire, OX11 0DE, UK.

[†]Present address: CIC nanoGUNE Consolider, Tolosa Hiribidea 76, E-20018 Donostia - San Sebastian, Spain.

*e-mail: ndm12@cam.ac.uk

We report a spin valve with a few-layer graphene flake bridging highly spin-polarised $La_{0.67}Sr_{0.33}MnO_3$ electrodes, whose surfaces are kept clean during lithographic definition. Sharp magnetic switching is verified using photoemission electron microscopy with X-ray magnetic circular dichroism contrast. A naturally occurring high interfacial resistance ~12 MΩ facilitates spin injection, and a large resistive switching (0.8 MΩ at 10 K) implies a 70-130 μm spin diffusion length that exceeds previous values ≤30 μm obtained with sharp-switching electrodes. This demonstration brings graphene spintronics one step closer to applications.

Graphene is at the centre of an ever-growing research effort, due to its unique properties [1]. In particular, it shows great potential in spintronics [2-5] because its spin diffusion length, l_{sf}^{G}, is expected to be long compared to semiconductors and metals, as a consequence of weak spin-orbit coupling and weak hyperfine interaction [4,6]. Significant progress has been made towards the realization of spintronic devices [5], but a better understanding of spin transport in graphene is required in order to realize logic and memory operations in which the spin degree of freedom is manipulated [7,8]. Here we will show that spin-polarized electrons can travel further in graphene than previously thought.

Spin transport has been previously measured in both graphene [2,9-12], graphite flakes [13-16] and hBN-encapsulated graphene [17]. By fitting Hanle curves [2] that describe the precession of transport spins in an out-of-plane magnetic field, a wide range of $l_{\mathrm{sf}}^{\mathrm{G}}$ values were reported in the literature at various temperatures, from 1 μm [15] up to 30 μm [17] (both measured at room tempertaure). The origin of the spin relaxation that limits $l_{\mathrm{sf}}^{\mathrm{G}}$ is still debated, and may be associated with impurities [18], ripples [6], substrates [19], and spin absorption in ferromagnetic electrodes [12,20,21].

Unwanted spin absorption arises in ferromagnetic electrodes if there is a 'conductivity mismatch' with respect to a non-magnetic channel, i.e. a discrepancy in the product of resistivity and spin diffusion length [22,23]. This problem can be avoided by inserting an insulating barrier between the two materials [23], e.g. with resistances in the range of a few MΩ for graphene with metallic electrodes [20]. By exploiting this approach, ref. [3] reported $l_{\mathrm{sf}}^{\mathrm{G}}$ ~ 150 μm in multilayer graphene, with the interfacial resistance (tens of MΩ) dominating the channel resistance (~1 kΩ). However, the magnetoresistance (*MR*) data in [3] showed quasi-continuous switching, incompatible with the parallel/antiparallel magnetic electrode configurations that were assumed when analyzing these data. Therefore the reported value of $l_{\mathrm{sf}}^{\mathrm{G}}$ may include contributions unrelated to spin transport, e.g. from tunneling anisotropic magnetoresistance (TAMR), which arises at contacts due to non-180° magnetic switching [24,25].

Here we report good spin transport in a mechanically exfoliated flake of five-layer graphene (5LG) that bridges two epitaxial electrodes of the ferromagnetic oxide $La_{0.67}Sr_{0.33}MnO_3$ (LSMO) to form an LSMO-5LG-LSMO spin valve. At 10 K, this device can be switched using a magnetic field to interconvert the low state of resistance R_P with the high state of resistance $R_{AP} = R_P + \Delta R$, which is visible above the background noise (ΔR ~ 0.8 MΩ, $MR = \Delta R/R_P$ ~ 3.0%). By contrast, previous reports based on these materials recorded no MR [26], or TAMR without spin transport [25]. Allowing the interfacial spin polarization γ to assume a wide range of values $0.95 > \gamma > 0.54$, cf. [27], the drift-diffusion model confirms long-distance spin transport at 10 K, with 70 μm < $l_{\mathrm{sf}}^{\mathrm{G}}$ < 130 μm.

The desired switching between parallel and antiparallel magnet electrode configurations is confirmed at 150 K, using photoemission electron microscopy (PEEM) with magnetic contrast from X-ray magnetic circular dichroism (XMCD) [28]. Magneto-optical Kerr effect (MOKE) microscopy confirms that our uniaxial in-plane magnetic easy axis does

not undergo any re-orientation on cooling to the transport measurement temperature of 10 K. Therefore our signal is due to spin transport, as intended.

The good spin transport arises for five reasons. First, LSMO possesses a high spin polarization of up to 100% at 5 K [29,30] (and is therefore commonly used in spintronic devices [27,31]). Second, our LSMO surfaces are kept clean during electrode definition with a temporary layer of Au, which is completely removed by chemical etching prior to FLG transfer. Third, by adopting the pseudocubic (110) orientation of LSMO, we are able to switch between parallel/antiparallel magnetic electrode configurations at distinct and well-defined magnetic fields, which is non-trivial for complex oxides [32]. This sharp switching is essential for estimating $l_{\mathrm{sf}}^{\mathrm{G}}$ without spurious effects, such as TAMR. Moreover, switching between single-domain states enhances spin signals [32]. Fourth, the insulating barriers required for good spin injection arise naturally from the structural and chemical discrepancy between the two materials. Fifth, flakes of few-layer graphene (FLG), whose physical properties represent an interpolation between two-dimensional single-layer graphene (SLG) and bulk graphite [33], possess larger values of $l_{\mathrm{sf}}^{\mathrm{G}}$ than SLG, due to increased screening from impurity scattering potentials [13-15].

Sample preparation is as follows. Two similar LSMO films are grown epitaxially by pulsed laser deposition (PLD) on un-terminated single crystals of $SrTiO_3$ (STO) (110) (as described in supplementary material [34]). The film used for the device and the MOKE studies is 30 nm thick. The film used for PEEM is slightly thicker (65 nm). Both have cube-on-cube epitaxy, are fully strained, and possess atomically flat surfaces between step terraces (Supplementary Figs S1-2). Vibrating sample magnetometry shows in-plane uniaxial magnetic anisotropy [35] collinear with $[001]_{\mathrm{STO}}$. The anisotropy constant is 43 kJ m^{-3} at 150 K, and 6.5 kJ m^{-3} at room temperature, similar to previous reports [36].

Similar electrodes are defined in both films by optical lithography and Ar-ion milling. For the PEEM sample, we avoid arcing by replacing the over-milled LSMO with 50 nm of sputter-deposited Au (using the electrode-definition mask as a lift-off mask prior to dissolution). For the spin-valve device/MOKE sample, we (1) reduce any tendency for 5LG to sag by replacing the over-milled LSMO with 48 nm of amorphous $NdGaO_3$ (NGO) deposited at room temperature by PLD (again, using the electrode-definition mask as a lift-off mask prior to dissolution); (2) ensure clean electrode surfaces by evaporating a 10 nm-thick protective Au layer prior to lithography, removing this layer in an aqueous KI/I_2

solution after lithography, and then wiping with cotton buds soaked in isopropanol; and (3) finally anneal in 55 kPa O_2 at 750 ˚C to avoid substrate conductivity.

FLG flakes are produced by micromechanical cleavage of natural graphite. A combination of optical contrast [37], Raman spectroscopy [38,39] and Atomic Force Microscopy (AFM) are used to identify 5LG flakes. These are then transferred onto LSMO electrodes by a wet transfer technique [1,40] (see supplementary materials [34]).

Magnetic switching of LSMO electrodes is studied at ~150 K using XMCD-PEEM (Fig. 1). The images are obtained at magnetic remanence after applying a magnetic field $\mu_0 H_{\text{pulse}}$ along the in-plane LSMO easy axis || $[001]_{\text{STO}}$ (red arrow, Fig. 1). The value of XMCD asymmetry represents the projection of the in-plane surface magnetization along the direction indicated by the green arrow (in-plane projection of the grazing-incidence beam) [32]. Regions of in-plane electrode magnetization lying parallel (antiparallel) to this green arrow appear blue (red). The initial application of a negative magnetic field leads to a homogeneously magnetized remanent state (Fig. 1a). The application of successively larger positive field pulses leads to magnetization reversal in individual electrodes (Fig. 1b,c), and ultimately magnetization reversal in all four electrodes (Fig. 1d). The subsequent application of successively larger negative field pulses leads to a second magnetization reversal in each electrode (Fig. 1e-h).

The electrode switching sequence is A, B, C+D in the up-sweep (Fig. 1a-d), and A, B, D, C in the down-sweep (Fig. 1e-h), differing only because the field steps in our up-sweep are too large to distinguish switching in C and D. This switching sequence (widest, narrowest, narrowest, intermediate) is incompatible with the monotonic dependence of switching field on electrode width that might be expected due to shape anisotropy. This suggests that there is a competition between more (fewer) nucleation sites and lower (higher) demagnetizing field in wider (narrower) electrodes. The sharp switching, which we exploit in our spintronic device, implies that domain-wall pinning is negligible, such that magnetization reversal is limited by domain nucleation.

MOKE microscopy is used to investigate magnetic switching in the widest LSMO electrode (A) at the 10 K magneto-transport measurement temperature (the sensitivity of the MOKE setup is not sufficient to reliably measure magnetic switching in the smaller electrodes). The magnetic easy axis of electrode A is collinear with $[001]_{\text{STO}}$ (Fig. 2), and the

perpendicular in-plane direction is a magnetically anhysteretic hard axis. These MOKE observations are consistent with our 150 K imaging study of all four electrodes (Fig. 1). The magnitude of the electrode A switching field measured by MOKE at 10 K ($|\mu_0 H|$ ~ 8 mT, Fig. 2) exceeds the corresponding value that may be inferred from our imaging study at 150 K ($|\mu_0 H|$ ~ 1.2-1.4 mT, Fig. 1), primarily because reducing temperature increases magnetic anisotropy, such that the nucleation field required for switching is higher [41].

The 5LG flake is positioned across all four LSMO electrodes A-D, as seen by AFM (upper inset, Fig. 2). The observed wrinkles are absent in a phase-contrast AFM image of the same area (lower inset, Fig. 2), implying that the flake is clean (i.e. no residual PMMA). The flake lies conformally on the LSMO electrodes, with sagging reduced due to the NGO deposited between electrodes.

Fig. 3 compares the 5LG Raman spectra before and after transfer, confirming successful transfer with no sample damage. The D peak is absent, implying a limited number of defects [37,39]. The Raman spectrum of STO (Fig. 3, green line) shows the expected peaks [42]. Since the D band of graphene and the LO_4 + LO_2 phonons of the STO substrate [42] both fall in the same range at ~1310 cm^{-1}, the Raman spectrum of the STO substrate is subtracted point-by-point from the spectrum of 5LG on STO (Fig. 3, red line) to confirm that the D band remains absent after transfer (Fig. 3, black line).

The two-terminal resistance between adjacent electrode pairs in the device at 10 K is R_{AB} ~ 10 MΩ, R_{BC} ~ 24 MΩ and R_{CD} ~ 150 MΩ (electrode spacings l_{AB} ~ 3 μm, l_{BC} ~ 2 μm and l_{CD} ~ 1 μm). Parasitic conduction through the substrate is excluded by measuring LSMO electrode pairs without 5LG, elsewhere on the same chip. The high values of resistance indicate that the LSMO-5LG interfaces function as tunnel barriers [25], consistent with non-linear current-voltage plots (Supplementary Fig. S3). Device resistance is dominated by these LSMO-5LG interfaces, whose resistance-area products vary by an order of magnitude. This variation implies inhomogeneous interfacial transport, possibly with local current densities that produce failure in a region too small or too deeply buried for AFM detection.

Measurements of R_{BC} (H) at 10K are obtained during three full cycles of applied magnetic field prior to device failure (Fig. 4, raw data in Supplementary Fig. S4). These data follow from measurements of over 20 devices. The noise in this device may arise at the LSMO-5LG interfaces because of intermittent contact, or electrochemical reactions induced

by Joule heating. Magnetically induced switching due to spin-valve behaviour produces two symmetric high-resistance plateaux in the range 12.5 mT < $|\mu_0 H|$ < 34.5 mT (Fig. 4b). Given the switching sequence seen in Fig. 1 at the higher temperature of 150 K, we infer that B switches at the lower field ($|\mu_0 H_B| \sim 12.5$ mT), while C switches at the higher field ($|\mu_0 H_C| \sim 34.5$ mT), with higher switching-field values at the lower temperature due to enhanced uniaxial magnetic anisotropy [35,36].

The two high-resistance states at 10 K differ from the low-resistance state $R_P = 24.8$ MΩ by $\Delta R \sim 0.8 \pm 0.2$ MΩ (Fig. 4) (B and C subscripts are dropped for analysis). This yields low-field $MR \sim 3.0 \pm 0.2\%$. Given that our electrodes display sharp 180° magnetization reversal (Figs 1-2), we deduce that the high-resistance states arise from spin transport through the 5LG, rather than TAMR or other effects linked to inhomogeneous magnetization. This spin transport at 10 K may be interpreted using the drift-diffusion model [23]:

$$\Delta R = \frac{2(\beta_{\mathrm{LSMO}} R_{\mathrm{LSMO}} + \gamma r_{\mathrm{b}}^{*})^2}{(r_{\mathrm{b}}^{*} + R_{\mathrm{LSMO}}) \cosh\left(\frac{L}{l_{\mathrm{sf}}^{\mathrm{G}}}\right) + \frac{R_{\mathrm{G}}}{2}\left[1 + (\frac{r_{\mathrm{b}}^{*}}{R_{\mathrm{G}}^{\mathrm{S}}})^2\right] \sinh(\frac{L}{l_{\mathrm{sf}}^{\mathrm{G}}})},$$

where $R_{\mathrm{LSMO}} = \frac{1}{1-\beta_{\mathrm{LSMO}}^2} \frac{\rho_{\mathrm{LSMO}} l_{\mathrm{sf}}^{\mathrm{LSMO}}}{wd}$ is the spin resistance of LSMO, $R_{\mathrm{G}}^{\mathrm{S}} = \rho_{\mathrm{S}}^{\mathrm{G}} \frac{l_{\mathrm{sf}}^{\mathrm{G}}}{w}$ is the spin resistance of 5LG, and $r_{\mathrm{b}}^{*} = \frac{R_P}{2(1-\gamma^2)}$ is the spin resistance of each LSMO-5LG interface (whose resistance $R_P/2 \sim 12$ MΩ dominates device resistance). In the above equations, β_{LSMO} is the bulk LSMO spin polarization, γ is the interfacial spin polarization, $l_{\mathrm{sf}}^{\mathrm{LSMO}}$ is the LSMO spin diffusion length, ρ_{LSMO} is the LSMO resistivity, d is the width that we assume to represent both LSMO electrodes separated by L, and w is the width of the 5LG flake with sheet resistance $\rho_{\mathrm{S}}^{\mathrm{G}}$.

Allowing unknown parameters $l_{\mathrm{sf}}^{\mathrm{G}}$ and γ to vary over a wide range of values, we plot contours of $MR = \Delta R/R_P$ at 10 K (Fig. 5) using $R_P = 24.8$ MΩ (Fig. 4b), $\beta_{\mathrm{LSMO}} = 0.95$ [29], a value of $l_{\mathrm{sf}}^{\mathrm{LSMO}} \approx 2.6$ nm [34] that is much smaller than $l_{\mathrm{sf}}^{\mathrm{G}}$ and therefore not critical, $\rho_{\mathrm{LSMO}} = 10^{-6}$ Ω m as measured for our films, $d = 6$ μm, $w = 7$ μm, and $\rho_{\mathrm{S}}^{\mathrm{G}} \approx 400$ Ω for our 5LG. If we assume $0.95 > \gamma > 0.54$ from spin-polarized tunnelling studies of LSMO [30,43] then the contour representing $MR = 3.0\%$ is shallow, such that $l_{\mathrm{sf}}^{\mathrm{G}}$ at 10 K length lies in a

narrow range between 70 μm (γ = 0.95) and 130 μm (γ = 0.54). Assuming γ = 0.8 as in [27] implies l_{sf}^{G} ~ 85 μm (red dot, Fig. 5).

At higher temperatures, our 10 K values of 70 μm ≤ l_{sf}^{G} ≤ 130 μm should not fall significantly given that l_{sf}^{G} has been reported to show a weak temperature dependence in both experimental [2,9,15] and theoretical [19] studies. Therefore we may directly compare our low-temperature values with the smaller experimental values of ≤30 μm, for graphitic flakes [13-15] and graphene [17], measured at various temperatures including room temperature. Although high interfacial resistance is required to limit spin absorption [12,20,21] in our LSMO electrodes, our interfacial resistance is so high that *MR* is suppressed. This is seen for the afore-mentioned choice of γ = 0.8, where approximately halving interfacial resistance to obtain R_P = 12.5 kΩ would increase *MR* to 170% (Fig. 5, inset).

Increasing *MR* is attractive for applications [44] because it leads to an increase of spin signal $V \times MR$, i.e. the voltage difference between parallel/antiparallel configurations for bias voltage *V*. Our experimental *MR* = 3.0% with *V* = 80 mV implies $V \times MR$ = 2.4 mV, whereas increasing *MR* to 170% would increase $V \times MR$ to 136 mV, exceeding the LSMO-MWNT-LSMO value of 65 mV deemed suitable for applications [27]. Note that our entire range 70 μm ≤ l_{sf}^{G} ≤ 130 μm exceeds the 50 μm deduced for MWNTs [27], possibly reflecting different sources of spin relaxation [45], e.g. FLG edges and MWNT curvature.

In summary, we have reported spin transport at 10 K through a five-layer graphene flake that forms resistive interfaces with highly spin-polarized LSMO (110) electrodes, using XMCD-PEEM imaging to confirm sharp magnetic switching in the electrodes. By assuming 0.95 > γ > 0.54, we infer values of 70 μm < l_{sf}^{G} < 130 μm that exceed all experimental values for graphitic flakes [13-15] and graphene [17] with sharp-switching electrodes. None of these experimental values should be severely compromised if measured at room temperature, as l_{sf}^{G} has been reported to show a weak temperature dependence [2,9,15,19]. The key future challenge is to increase *MR* by reducing interfacial resistance, but annealing in forming gas [46] or using a current [47] would degrade the LSMO. Dry graphene transfer [48] could yield the desired reduction, whilst also increasing l_{sf}^{G} through increased cleanliness.

Acknowledgements. This work was funded by grant F/09 154/E from the Leverhulme Trust, a Schlumberger Cambridge International Scholarship, a UK EPSRC DTA award, the Royal Society (X. M.), the EU Graphene Flagship (no. 604391), ERC Grant Hetero2D, EPSRC Grants EP/K01711X/1, EP/K017144/1, EP/N010345/1, EP/M507799/1 and EP/L016087/1, and Wolfson College. We acknowledge Diamond Light Source for time on beamline I06 under proposal SI-8325.

References

1. A. C. Ferrari *et al.*, Nanoscale **7**, 4598 (2015).
2. N. Tombros, C. Jozsa, M. Popinciuc, H. T. Jonkman and B. J. van Wees, Nature **448**, 571 (2007).
3. B. Dlubak, M.-B. Martin, C. Deranlot, B. Servet, S. Xavier, R. Mattana, M. Sprinkle, C. Berger, W. A. de Heer, F. Petroff, A. Anane, P. Seneor and A. Fert, Nature Phys. **8**, 557 (2012).
4. D. Pesin and A. H. MacDonald, Nature Mater. **11**, 409 (2012).
5. W. Han, R. K. Kawakami, M. Gmitra and J. Fabian, Nature Nanotech. **9**, 794 (2014).
6. D. Huertas-Hernando, F. Guinea and A. Brataas, Phys. Rev. Lett. **103**, 146801, (2009).
7. S. Datta and B. Das, Appl. Phys. Lett. **56**, 665 (1990).
8. B. Behin-Aein, D. Datta, S. Salahuddin and S. Datta, Nature Nanotech. **5**, 266 (2010).
9. T. –Y. Yang, J. Balakrishnan, F. Volmer, A. Avsar, M. Jaiswal, J. Samm, S. R. Ali, A. Pachoud, M. Zeng, M. Popinciuc, G. Güntherodt, B. Beschoten and B. Özyilmaz, PRL. **107**, 047206 (2011).
10. I. Neumann, M. V. Costache, G. Bridoux, J. F. Sierra and S. O. Valenzuela, Appl. Phys. Lett. **103**, 112401 (2013).
11. M. V. Kamalakar, C. Groenveld, A. Dankert and S. P. Dash, Nat. Commun. 6: 6766 (2015). doi: 10.1038/ncomms7766 .
12. F. Volmer, M. Drögeler, E. Maynicke, N. von den Driesch, M. L. Boschen, G. Güntherodt, C.Stampfer and B. Beschoten, Phys. Rev. B **90**, 165403 (2014).
13. Y. Gao, Y. J. Kubo, C. -C. Lin, Z. Chen and J. Appenzeller, Electron Devices Meeting (IEDM), 2012 IEEE International, 4.4.1 (2012).
14. H. Goto, A. Kanda, T. Sato, S. Tanaka, Y. Ootuka, S. Odaka, H. Miyazaki, K. Tsukagoshi and Y. Aoyagi, Appl. Phys. Lett. **92**, 212110 (2008).
15. T. Maassen, F. K. Dejene, M. H. D. Guimarães, C. Józsa and B. J. van Wees, Phys. Rev. B **83**, 115410 (2011).
16. M. Shiraishi, M. Ohishi, R. Nouchi, N. Mitoma, T. Nozaki, T. Shinjo and Y. Suzuki, Adv. Funct. Mater. **19**, 3711 (2009).
17. M. Drögeler, C. Franzen, F. Volmer, T. Pohlmann, L. Banszerus, M. Wolter, K. Watanabe, T. Taniguchi, C. Stampfer and B. Beschoten. Nano Lett. **16**, 3533 (2016).
18. K. Pi, W. Han, K. M. McCreary, A. G. Swartz, Y. Li and R. K. Kawakami, Phys.

Rev. Lett. **104**, 187201 (2010).
19. C. Ertler, S. Konschuh, M. Gmitra and J. Fabian, Phys. Rev. B **80,** 041405 (2009).
20. H. Idzuchi, A. Fert and Y. Otani, Phys. Rev. B **91**, 241407(R) (2015).
21. M. V. Kamalakar, A. Dankert, J. Bergsten, T. Ive and S. P. Dash, Sci Rep. 4: 6146 (2014), doi: 10/ 1038/srep06146.
22. G. Schmidt, D. Ferrand, L. W. Molenkamp, A. T. Filip, and B. J. van Wees. Phys. Rev. B **62**, R4790 (2000).
23. A. Fert and H. Jaffrès. Phys. Rev. B **64**,184420 (2001).
24. C. Gould, C. Rüster, T. Jungwirth, E. Girgis, G. M. Schott, R. Giraud, K. Brunner, G. Schmidt and L. W. Molenkamp, Phys. Rev. Lett. **93**, 117203 (2004).
25. L. C. Phillips, A. Lombardo, M. Ghidini, W. Yan, S. Kar-Narayan, S. J. Hämäläinen, M. Barbone, S. Milana, S. van Dijken, A. C. Ferrari and N. D. Mathur, Appl. Phys. Lett., **108**,112405 (2016).
26. M. Rocci, J. Tornos, A. Rivera-Calzada, Z. Sefrioui, M. Clement, E. Iborra, C. Leon and J. Santamaria, Appl. Phys. Lett. **104**, 102408 (2014).
27. L. E. Hueso, J. M. Pruneda, V. Ferrari, G. Burnell, J. P. Valdés-Herrera, B. D. Simons, P. B. Littlewood, E. Artacho, A. Fert and N. D. Mathur, Nature **445**, 410 (2007).
28. C. M. Schneider and G. Schönhense, Rep. Prog. Phys. **65**, R1785 (2002).
29. J. -H. Park, E. Vescovo, H. -J. Kim, C. Kwon, R. Ramesh and T. Venkatesan, Nature **392**, 794 (1998).
30. M. Bowen, A. Barthélémy, M. Bibes, E. Jacquet, J. –P. Contour, A. Fert, F. Ciccacci, L. Duò and R. Bertacco, Phys. Rev. Lett. **95**, 137203 (2005).
31. V. Garcia, M. Bibes, L. Bocher, S. Valencia, F. Kronast, A. Crassous, X. Moya, S. Enouz-Vedrenne, A. Gloter, D. Imhoff, C. Deranlot, N. D. Mathur, S. Fusil, K. Bouzehouane and A. Barthélémy, Science **327**, 1106 (2010).
32. L. C. Phillips, W. Yan, X. Moya, M. Ghidini, F. Maccherozzi, S. S. Dhesi and N. D. Mathur. Phys. Rev. Applied **4**, 064004 (2015).
33. A. H. Castro Neto, F. Guinea, N. M. R. Peres, K. S. Novoselov and A. K. Geim, Rev. Mod. Phys. **81**, 109 (2009).
34. Supplementary material describes methods, presents raw electrical data, and calculates the spin diffusion length in LSMO.
35. W. Yan, PhD thesis, University of Cambridge (2014).
36. H. Boschker, J. Kautz, E. P. Houwman, G. Koster, D. H. A. Blank and G. Rijnders,

J. Appl. Phys. **108**, 103906 (2010).

37. C. Casiraghi, A. Hartschuh, E. Lidorikis, H. Qian, H. Harutyunyan, T. Gokus, K. S. Novoselov and A. C. Ferrari, Nano Lett. **7**, 2711 (2007).
38. A. C. Ferrari, J. C. Meyer, V. Scardaci, C. Casiraghi, M. Lazzeri, F. Mauri, S. Piscanec, D, Jiang, K. S. Novoselov, S. Roth and A. K. Geim, Phys. Rev. Lett. **97**, 187401 (2006).
39. A. C. Ferrari and D. M. Basko, Nature Nanotech. **8**, 235 (2013).
40. F. Bonaccorso, A. Lombardo, T. Hasan, Z. Sun, L. Colombo and A. C. Ferrari, Materials Today **15**, 564 (2012).
41. K. -D. Durst and H. Kronmüller, J. Magn. Magn. Mater. **68**, 63 (1987).
42. W. G. Nilsen and J.G. Skinner, J. Chem. Phys. **48**, 2240 (1968).
43. Y. Lu, X. W. Li, G. Q. Gong, G. Xiao, A. Gupta, P. Lecoeur, J. Z. Sun, Y. Y. Wang and V. P. Dravid, Phys. Rev. B **54**, R8357 (1996).
44. I. Žutić, J. Fabian and S. Das Sarma, Rev. Mod. Phys. **76**, 323 (2004).
45. D. Huertas-Hernando, F. Guinea and A. Brataas, Phys. Rev. B **74**, 155426, (2006).
46. M. Ishigami, J. H. Chen, W. G. Cullen, M. S. Fuhrer and E. D. Williams, Nano Lett. **7**, 1643 (2007).
47. T. Taychatanapat, PhD thesis, Harvard University (2013).
48. B. Hunt, J. D. Sanchez-Yamagishi, A. F. Young, M. Yankowitz, B. J. LeRoy, K. Watanable, T. Taniguchi, P. Moon, M. Koshino, P. Jarillo-Herrero and R. C. Ashoori, Science **340**, 1427 (2013).

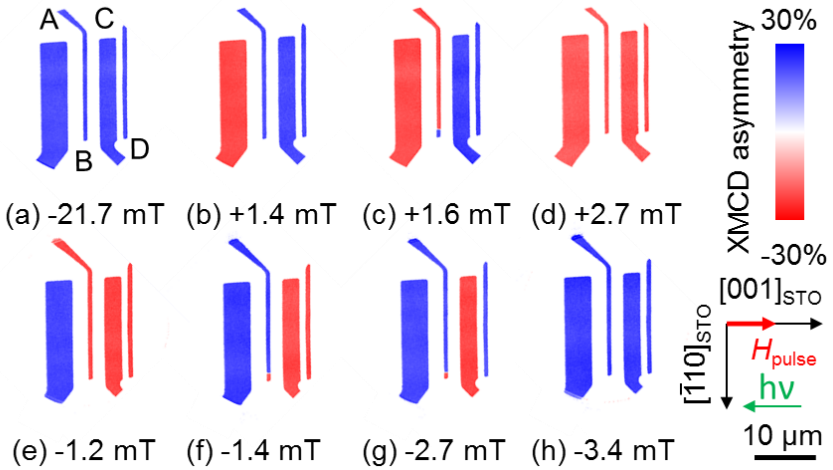

Figure 1. Magnetic switching in LSMO (110) electrodes A-D at 150 K. (a-h) PEEM images obtained at remanence after applying magnetic field $\mu_0 H_{\text{pulse}}$ along the LSMO easy axis || $[001]_{\text{STO}}$ (red arrow). Field magnitudes represent upper bounds on the fields at which the observed switching occurred. XMCD asymmetry represents the projection of the in-plane surface magnetization on the in-plane projection of grazing-incidence beam direction (green arrow). Blue (red) depicts magnetization parallel (antiparallel) to the green arrow. Transport is measured between B and C using similar electrodes.

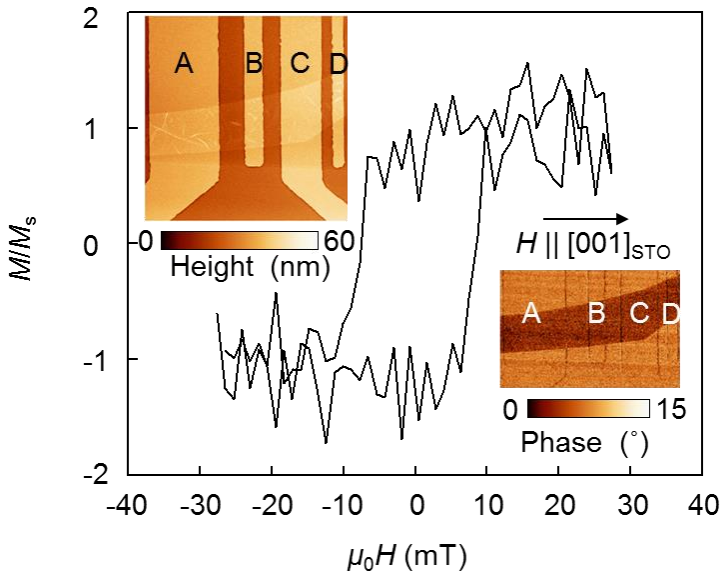

Figure 2. LSMO-5LG-LSMO spin-valve characterization. MOKE microscopy measurements of magnetic switching in LSMO (110) electrode A at 10 K. The applied magnetic field $\mu_0 H$ and the measured component of magnetization M were collinear with the LSMO easy axis and $[001]_{STO}$. M_s is saturation magnetization. AFM image (30 μm × 30 μm) (upper inset) and phase-contrast AFM image (lower inset) show FLG flake. Device failure is not apparent in the images here, which are obtained after collecting the transport data of Fig. 4 using electrodes B and C.

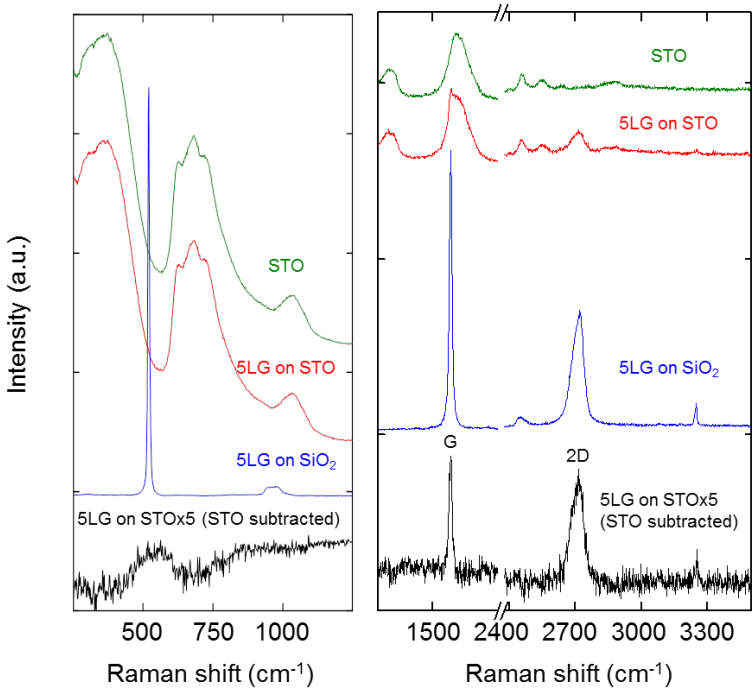

Figure 3. Raman spectra of the graphene flake before and after transfer. G and 2D peaks are visible for the flake on SiO_2 (blue) and after subsequent transfer to LSMO electrodes on STO (red). A point-by-point subtraction of the STO background (green) yields the spectrum for the graphene flake on STO (black), where the D peak is absent. Panel (a) shows the spectra between 250 cm^{-1} and 1250 cm^{-1}, while panel (b) shows the spectra between 1250 cm^{-1} and 3500 cm^{-1}.

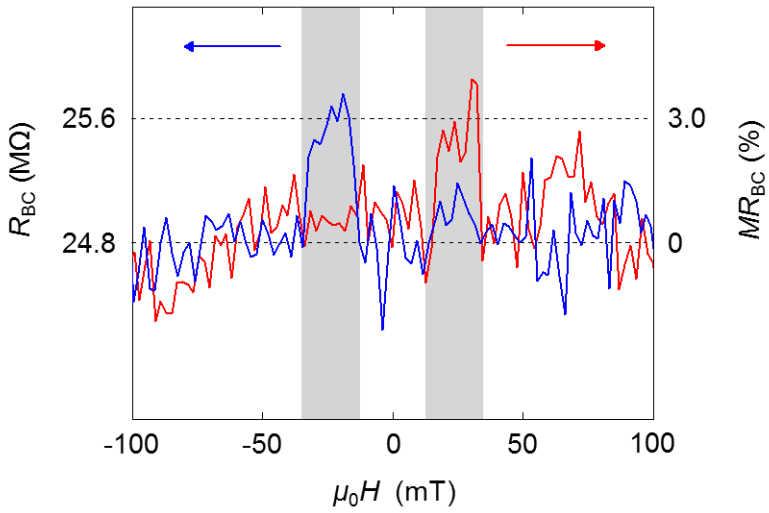

Figure 4. LSMO-5LG-LSMO spin-valve magnetotransport at 10 K. Resistance R_{BC} and magnetoresistance MR_{BC} on decreasing (blue) and increasing (red) magnetic field H along the LSMO easy axis collinear with $[001]_{STO}$. Dashed lines indicate $R_{BC} = 24.8$ MΩ and $R_{BC} + \Delta R_{BC} = 25.6$ MΩ for parallel and antiparallel electrode magnetizations, respectively. Transition to antiparallel configuration indicated by grey shading in 12.5 mT < $|\mu_0 H|$ < 34.5 mT. Data obtained for five-layer flake, spanning 2 μm gap between electrodes B-C, after averaging three up and down sweeps (Supplementary Fig. S4). Bias voltage = 80 mV. B and C electrode subscripts dropped for analysis.

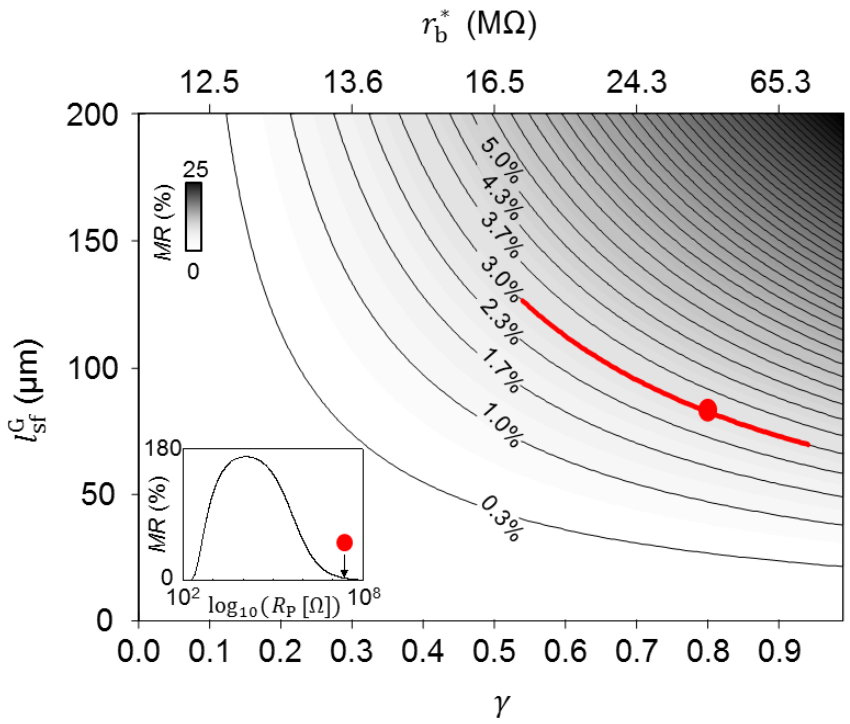

Figure 5. LSMO-5LG-LSMO spin-valve parameters at 10 K. Contours and greyscale showing $MR(\gamma, l_{sf}^G)$ from the drift-diffusion model [23]. For $MR \sim 3.0\%$ and $0.95 > \gamma > 0.54$ we find 70 μm < l_{sf}^G < 130 μm (red contour). Red dot denotes $MR(\gamma = 0.8, l_{sf}^G = 85\ \mu m) = 3.0\%$ for experimental value of R_P = 24.8 MΩ. Inset: $MR(R_P)$ for $\gamma = 0.8$ and $l_{sf}^G = 85$ μm.

Supplementary information

for

Long spin diffusion length in few-layer graphene flakes

W. Yan[1†], L. C. Phillips[1], M. Barbone[2], S. Hämäläinen[3], A. Lombardo[2], M. Ghidini[1,4], X. Moya[1], F. Maccherozzi[5], S. van Dijken[3], S. S. Dhesi[5], A. C. Ferrari[2] and N. D. Mathur[1,*]

[1]Department of Materials Science, University of Cambridge, Cambridge, CB3 0FS, United Kingdom.

[2]Cambridge Graphene Centre, University of Cambridge, Cambridge CB3 0FA, United Kingdom.

[3]NanoSpin, Department of Applied Physics, Aalto University School of Science, P.O. Box 15100, FI-00076 Aalto, Finland.

[4]DiFeST,University of Parma, viale G.P. Usberti 7/A, 43124 Parma, Italy.

[5]Diamond Light Source, Chilton, Didcot, Oxfordshire, OX11 0DE, UK.

[†]Present address: CIC nanoGUNE Consolider, Tolosa Hiribidea 76, E-20018 Donostia - San Sebastian, Spain.

*e-mail: ndm12@cam.ac.uk

Film growth. Three similar LSMO films are grown epitaxially at 775 °C, in a flowing oxygen ambient of 15 Pa, from a stoichiometric target (Praxair) onto $SrTiO_3$ (110) substrates (Crystal GmbH) by pulsed laser deposition at 1 Hz using a KrF laser (Lambda Physik Compex 201, 248 nm, target-sample distance 8 cm).

For PEEM, we use a 65 nm-thick film that is grown at 0.41 ± 0.03 Å $pulse^{-1}$ with a fluence of 2.0 J cm^{-2}. For the LSMO-FLG-LSMO device and x-ray diffraction, we use two 30 nm films that are grown at 0.07± 0.01 Å $pulse^{-1}$, via a 15 mm × 4.5 mm aperture at the laser exit, with a fluence of 1.7 J cm^{-2}, and a spot size of 3.8 mm^2.

After deposition, the samples are annealed in ~55 kPa O_2 at 750 °C for 1 hour, before cooling to room temperature.

Film topography is studied using an AFM (Digital Instruments Nanoscope III) in tapping mode. Fig. S1 shows step-terraces on the surface of one of the 30 nm-thick films.

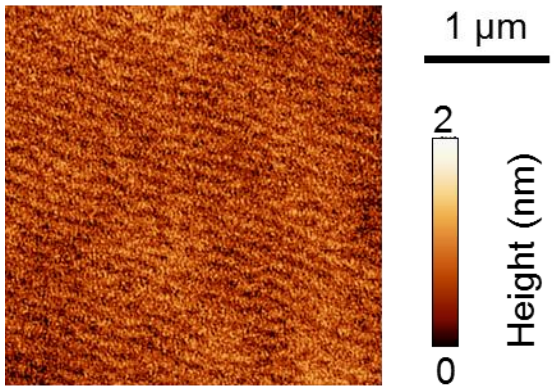

Fig S1. AFM image of one of the 30 nm-thick films.

X-ray film diffraction is performed using a PANalytical PW3050/65 X'pert PRO high-resolution diffractometer. The two panels in Fig. S2(a) show that the film is fully strained along both in plane directions, i.e. along [001] and $[\bar{1}10]$.

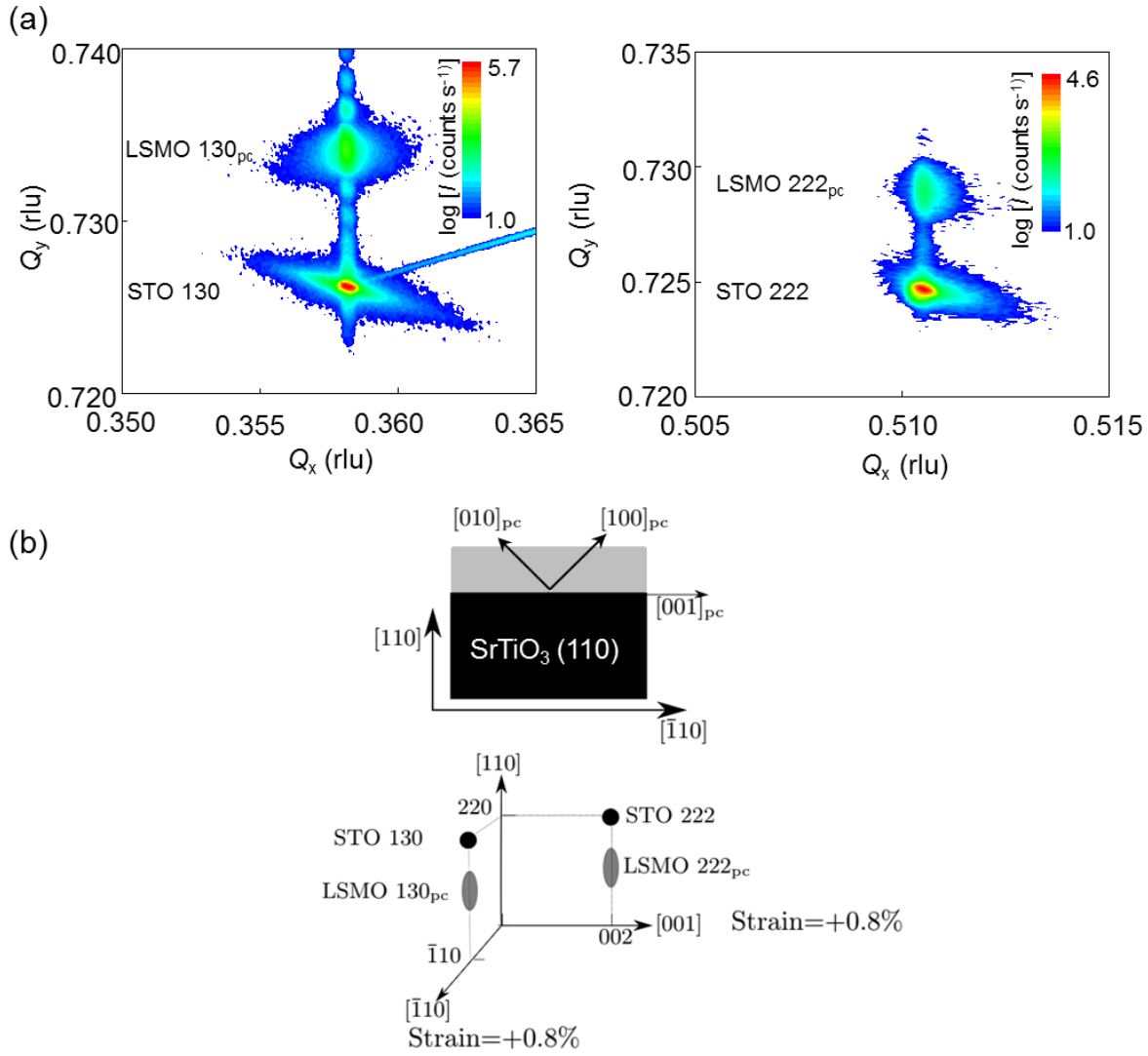

Fig S2. (a) Reciprocal space maps of a 30 nm-thick LSMO film with the in-plane projection of the incident X-ray beam parallel to [001] (left panel) and $[\bar{1}10]$ (right-panel). X-ray intensity is denoted *I* (current is denoted *I* in the main paper). (b) Schematic of film and substrate geometry.

XMCD-PEEM imaging of LSMO electrodes at ~150 K is performed at the Diamond Light Source beamline I06 with the X-ray beam at a grazing incidence angle of 16°, using an Elmitec SPELEEM-III microscope to image the local zero-field magnetization to a probe depth of ~7 nm and a typical lateral resolution of ~50 nm. After imaging with right (+) and left (-) circularly polarized light, we calculate X-ray absorption spectroscopy (XAS) $\left(I^{+}+I^{-}\right)$ and XMCD asymmetry $\left(I^{+}-I^{-}\right)/\left(I^{+}+I^{-}\right)$ for each pixel, where the influence of inhomogeneous illumination is avoided by evaluating $I^{\pm}=\left(I_{\mathrm{on}}^{\pm}-I_{\mathrm{off}}^{\pm}\right)/I_{\mathrm{off}}^{\pm}$, which is the relative intensity of secondary-electron emission arising from X-ray absorption on ($I_{\mathrm{on}}^{\pm}$ at 639.5 eV) and off ($I_{\mathrm{off}}^{\pm}$ at 630 eV) the Mn L_3 edge. Images for each x-ray energy and beam polarization are acquired during 10 s exposure times. Pulses of magnetic field are applied along the in-plane easy axis, between measurements at magnetic remanence, via a coil on the sample cartridge.

MOKE microscopy of LSMO electrodes is performed at 10 K using an imaging system from Evico Magnetics with a continuous-flow He cryostat (Janis ST-500). The measurements are conducted in longitudinal Kerr geometry (in-plane magnetic field parallel to the plane of incident light). Magnetic hysteresis curves of electrode A are obtained by using the microscope software to restrict data collection to the area of the electrode. Linear Faraday contributions from the cryostat cover glass and the microscope objectives are removed after data collection.

Graphene production and transfer. FLG is produced by micromechanical cleavage of natural graphite (NGS Naturgraphit) onto oxidized silicon wafers with oxide thickness of 285 nm and characterized by a combination of optical contrast [S1] and Raman spectroscopy [S2,S3]. Selected crystals are removed from the Si/SiO_2 substrate and deterministically placed onto LSMO electrodes by a wet transfer technique based on a polymethil methacrylate (PMMA) sacrificial layer. The polymer is spin coated onto the Si/SiO_2 substrate, then immersed in de-ionized (DI) water at 90 °C [S4]. The water intercalates at the SiO_2/PMMA interface and detaches the PMMA. Graphene flakes remain attached to the bottom of the PMMA layer and this is placed on the magnetic LSMO electrodes. In order to reduce the presence of water at the LSMO-graphene interface, the PMMA+graphene film is moved to a water-ethanol solution (1:4 ratio in volume) prior to placing on LSMO electrodes. Alignment is achieved by moving the PMMA+graphene film on the target substrate before evaporation of the ethanol-water solution. Success of the transfer is confirmed by optical microscopy, atomic force microscopy (AFM) and Raman spectroscopy.

Raman spectroscopy

Raman measurements are performed using a Renishaw InVia micro-spectrometer equipped with a $\times$100 objective (numerical aperture, N.A. = 0.85), a laser excitation wavelength of 514.5 nm, with laser spot size ~1 um and power <1 mW to avoid heating.

Magnetotransport measurements are performed using a Janis Research Supertran-VP cryostat with a continuous flow of liquid He. Bias voltage *V* is applied via mini-coax cables, and current *I* is measured using a Keithley 6487 picoammeter (Fig. S3). Fig. 4 was constructed using the raw data shown in Fig. S4, where at each measurement field the differential resistance $R = \Delta V/\Delta I$ was calculated for changes of *V* between 50 and 80 mV.

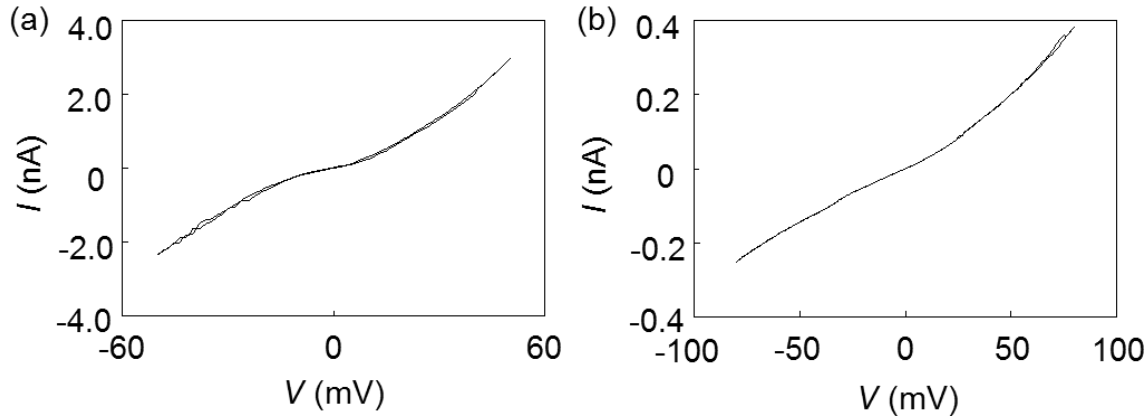

Fig. S3. *I*-*V* characteristics for electrodes (a) A-B and (b) C-D at 10 K.

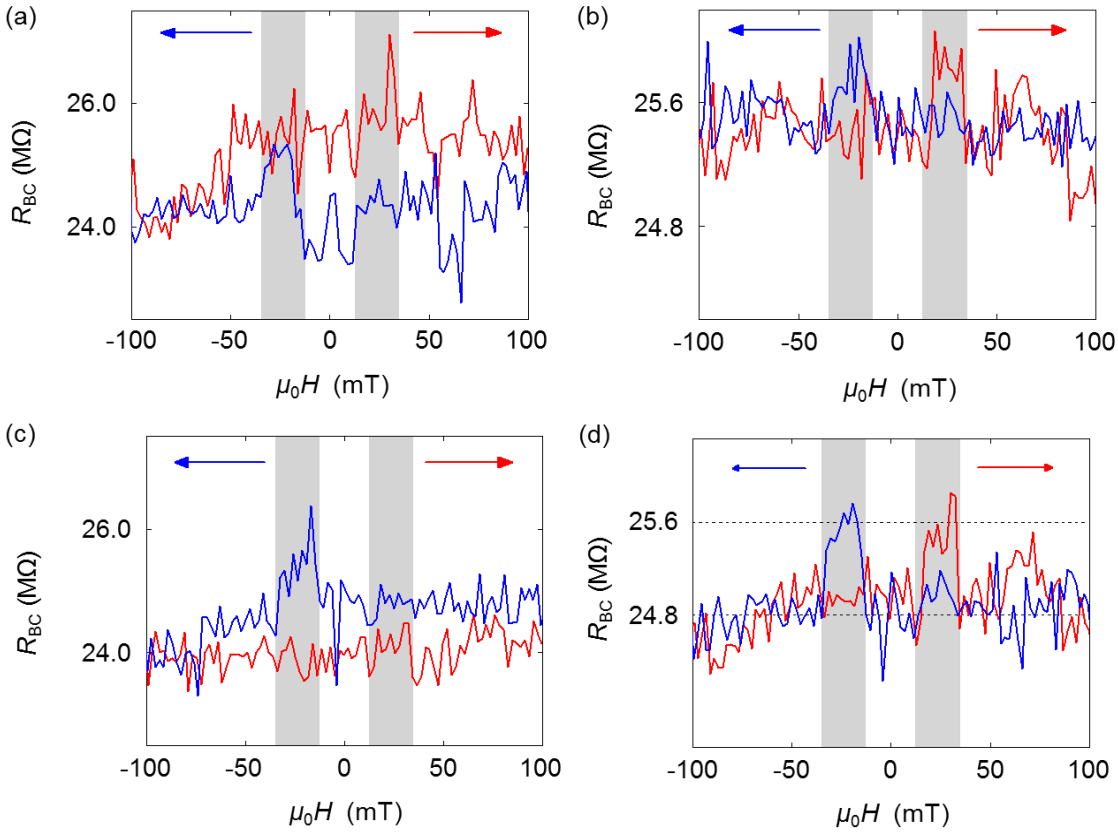

Fig. S4. (a) First, (b) second, (c) third field sweep used to construct Fig. 4 in the main paper, reproduced here in (d). Each down sweep precedes the subsequent up sweep. Grey shading in 12.5 mT < $|\mu_0 H|$ < 34.5 mT indicates transition to antiparallel electrode configuration.

Spin diffusion length in LSMO

The spin diffusion length $l_{\mathrm{sf}}^{\mathrm{LSMO}} = \sqrt{D_{\mathrm{LSMO}}\tau_{\mathrm{sf}}^{\mathrm{LSMO}}}$, where the spin relaxation time $\tau_{\mathrm{sf}}^{\mathrm{LSMO}}$ = 20 ps [S5] and spin diffusivity $D_{\mathrm{LSMO}} = \mu_{\mathrm{LSMO}} k_{\mathrm{B}} T$ depends on mobility $\mu_{\mathrm{LSMO}} = \sigma_{\mathrm{LSMO}} R_{\mathrm{H}}^{\mathrm{LSMO}}$. For LSMO, conductivity $\sigma_{\mathrm{LSMO}} \approx 10^{6}\ \Omega^{-1}\mathrm{m}^{-1}$ [S6], Hall coefficient $R_{\mathrm{H}}^{\mathrm{LSMO}} = 0.4\times10^{-3}$ cm^3 C^{-1} [S7] and $k_{\mathrm{B}} = 8.6173324 \times 10^{-5}$ eV K^{-1}, such that mobility $\mu_{\mathrm{LSMO}} = 0.4 \times 10^{-3}$ m^2 Ω^{-1} C^{-1}, and therefore $l_{\mathrm{sf}}^{\mathrm{LSMO}} \approx 2.6$ nm at T = 10 K.

References

[S1] C. Casiraghi, A. Hartschuh, E. Lidorikis, H. Qian, H. Harutyunyan, T. Gokus, K. S. Novoselov, and A. C. Ferrari, Nano Lett. **7**, 2711 (2007).

[S2] A. C. Ferrari, J. C. Meyer, V. Scardaci, C. Casiraghi, M. Lazzeri, F. Mauri, S. Piscanec, D, Jiang, K. S. Novoselov, S. Roth and A. K. Geim, Phys. Rev. Lett. **97**, 187401 (2006).

[S3] A. C. Ferrari and D. M. Basko, Nat. Nanotech. **8**, 235 (2013).

[S4] F. Bonaccorso, A. Lombardo, T. Hasan, Z. Sun, L. Colombo, and A. C. Ferrari, Mater. Today **15**, 564 (2012)

[S5] A. I. Lobad, R. D. Averitt, C. Kwon and A. J. Taylor, Appl. Phys. Lett. **77**, 4025 (2000).

[S6] L. E. Hueso, J. M. Pruneda, V. Ferrari, G. Burnell, J. P. Valdés-Herrera, B. D. Simons, P. B. Littlewood, E. Artacho, A. Fert and N. D. Mathur, Nature **445**, 410 (2007).

[S7] A. Asamitsu and Y. Tokura, Phys. Rev. B **58**, 47 (1998).